Thin Solid Films 520 (2012) 1745–1750

Contents lists available at SciVerse ScienceDirect

Thin Solid Films

journal homepage: www.elsevier.com/locate/tsf

Growth mode transition of atomic layer deposited Al_2O_3 on porous TiO_2 electrodes of dye-sensitized solar cells

Ta-Chang Tien [a,*], Fu-Ming Pan [a,*], Lih-Ping Wang [b,c], Feng-Yu Tsai [d], Ching Lin [d]

[a] Department of Materials Science and Engineering, National Chiao Tung University, Hsingchu, 300, Taiwan, ROC
[b] Green Energy & Environment Research Laboratories, Industrial Technology Research Institute, Hsingchu, 310, Taiwan, ROC
[c] Nanotechnology Research Center, Industrial Technology Research Institute, Hsingchu, 310, Taiwan, ROC
[d] Department of Materials Science and Engineering, National Taiwan University, Taipei, 106, Taiwan, ROC

ARTICLE INFO

Article history:
Received 15 December 2010
Received in revised form 16 August 2011
Accepted 16 August 2011
Available online 23 August 2011

Keywords:
Growth mode
Atomic layer deposition (ALD)
Core/shell nanoparticle
Dye-sensitized solar cells

ABSTRACT

This study investigates the growth behavior of atomic-layer-deposited (ALD) Al_2O_3 overlayers on porous TiO_2 electrodes, which comprise an anatase nanoparticle layer and a rutile particle layer, for optimizing dye-sensitized solar cells. The growth mode of the ALD Al_2O_3 overlayers changes from island growth to layer-by-layer growth during the first few ALD reaction cycles, and the growth mode transition is much more pronounced for the anatase electrode layer. The transition is likely a result of the reduction in the contractive lattice strain of the TiO_2 nanoparticles. The lattice strain in the hydroxylated TiO_2 nanoparticles is progressively reduced during the ALD Al_2O_3 deposition, resulting in the growth mode transition.

1. Introduction

Dye-sensitized solar cells (DSSCs) are potential candidates for third-generation renewable energy sources, primarily because of their low manufacturing costs and high cell efficiency (ca. 11%) [1,2]. The power conversion efficiency (PCE) of DSSCs based on nanoporous TiO_2 electrodes can be increased by 10–50% when Al_2O_3 overlayers are deposited on the electrodes [3–5]. The improved performance of DSSCs featuring Al_2O_3 overlayers is believed to result from reduction in the charge recombination rate at the interface between the dye and the TiO_2 electrode. But the thickness of the uniform Al_2O_3 overlayer should be thin enough so that charge transfer through the overlayer will not be hampered because the efficiency of the charge transfer due to tunneling effect exponentially decays with the thickness [6–8]. The increases in PCEs of dye-sensitized TiO_2 solar cells have been explained by considering the interfacial energy levels of the Al_2O_3 overlayers [9], i.e., the high recombination energy barrier at the Al_2O_3–TiO_2 interface, the large work function of the Al_2O_3 overlayers, and the low energy barrier between the dye and Al_2O_3. The Al_2O_3–TiO_2 interface in DSSCs can be optimized using various coating procedures; the sol–gel process, in particular, provides the capability of infiltrating the porous structures, thereby ensuring good coverage of the surface of the nanoporous electrode. Because the sol–gel process requires a sintering step, typically at 450–500 °C, to ensure good quality, it has limited compatibility with low-temperature fabrication processes, such as those employed to prepare plastic-based flexible DSSCs [10]. Although Haque et al. have deposited low-temperature (100 °C) sol–gel Al_2O_3 layers onto flexible DSSCs [11], the improvement in performance was less pronounced than that achieved using high-temperature sol–gel processes. In addition to the temperature constraints of the typical sol–gel process, the thickness of the sol–gel films can be altered with a resolution down to only ca. 1 nm [12,13], which is too coarse for adjusting the optimal thickness of the Al_2O_3 layers.

It is generally believed that, compared with sol–gel processes, atomic layer deposition (ALD) can form an Al_2O_3–TiO_2 heterostructure of better interfacial properties because it offers high deposition conformability [14], low deposition temperatures (down to 33 °C for Al_2O_3) [15], and high resolution (ca. 0.1 nm for Al_2O_3) in controlling the film thickness [16,17]. Thus, as an alternative to sol–gel processing, ALD may provide a significant opportunity to enhance the PCEs of DSSCs by providing Al_2O_3 overlayers on TiO_2 electrodes. However, the ALD process may not provide much of an advantage over high-temperature sol–gel techniques because of the low coverage of ALD Al_2O_3 overlayers on nanoporous TiO_2 electrodes [9,18]. This situation arises from the island-mode growth mechanism of the ALD Al_2O_3 overlayers, which results in a low coverage of overlayers on nanoporous TiO_2 electrodes. In this study, we investigated the growth mode and the optimal thickness of the Al_2O_3 overlayer on the porous TiO_2 electrode

* Corresponding authors. Tel.: +886 3 5915299; fax: +886 3 5820262.
E-mail addresses: tien@itri.org.tw (T.-C. Tien), fmpan@faculty.nctu.edu.tw (F.-M. Pan).

0040-6090/$ – see front matter © 2011 Elsevier B.V. All rights reserved.
doi:10.1016/j.tsf.2011.08.057

so that the PCE of DSSCs featuring the Al_2O_3/TiO_2 electrode can be further optimized.

2. Experimental details

The structure of the DSSCs is schematically shown in Fig. 1; the fabrication method has been described in detailed in previous works [18]. The TiO_2 electrodes had a diameter of 6 mm and comprised two screen-printed layers: a 12 μm-thick nanoporous layer at the bottom formed from anatase TiO_2 nanoparticles (ca. 20 nm) and a 4 μm-thick porous layer at the top formed from rutile TiO_2 particles having sizes in the range 200–400 nm. The smaller TiO_2 nanoparticles were prepared using a previously reported method [19]. The larger rutile TiO_2 particles were purchased from DuPont (Ti-Pure R-706).

Atomic layers of Al_2O_3 were deposited on the TiO_2 electrodes at 150 °C, using a Cambridge NanoTech Savannah 100 ALD system with trimethylaluminum (TMA) and H_2O as the precursors. The ALD process comprised a given number of identical cycles, each involving the following six steps: (i) dosing with H_2O for 0.05 s; (ii) soaking in the H_2O dose for 2 min; (iii) evacuating for 5 min; (iv) dosing with TMA by opening the TMA valve for 0.05 s; (v) soaking in the TMA dose for 2 min; and (vi) evacuating for 5 min. Both the TMA and H_2O precursors were introduced into the ALD chamber with the N_2 carrier gas at a flow rate of 20 sccm (precursor: $N_2 = 1:10$); the equivalent dose of TMA and N_2 was 4.0×10^{16} molecules for each ALD cycle. The temperature of the reactor wall was maintained at 200 °C to avoid gas adsorption on the wall during the ALD process.

Microstructure analysis of the TiO_2 electrodes was performed using a field-emission transmission electron microscope (TEM, JEOL, JEM-2100f) X-ray photoelectron spectroscopy (XPS) analysis of the TiO_2 electrodes was performed with an electron spectrometer (VG ESCAlab 250) using the Al Kα source (1486.6 eV). The lattice structure of the samples was studied by an X-ray diffractometer (Philips-PW3710) operated at a scanning step of 0.02°/s.

3. Results and discussion

The deposition of Al_2O_3 overlayers on a titania substrate, using Al $(CH_3)_3$ and H_2O as the precursors, can be separated into two consecutive stages: (1) the aluminum hydroxide formation on the titania surface and (2) the continuing Al_2O_3 growth. The first stage is represented by the following reactions:

$$Ti{-}OH^* + Al(CH_3)_3 \rightarrow Ti{-}O{-}Al(CH_3)_2^* + CH_4 \quad (1)$$

$$Ti{-}O{-}Al(CH_3)_2^* + 2H_2O \rightarrow Ti{-}O{-}Al(OH)_2^* + 2CH_4 \quad (2)$$

where the asterisks denote the surface species. Likewise, the continuing growth of the Al_2O_3 overlayer can be summarized by the two consecutive reaction steps [20]:

$$Al{-}OH^* + Al(CH_3)_3 \rightarrow Al{-}O{-}Al(CH_3)_2^* + CH_4 \quad (3)$$

$$Al{-}O{-}Al(CH_3)_2^* + 2H_2O \rightarrow Al{-}O{-}Al(OH)_2^* + 2CH_4 \quad (4)$$

where again the asterisks indicate surface species. According to the above reaction equations, at the end of each ALD reaction cycle, the sample is covered by hydroxyl surface groups. Noted that Eqs. 1–4 describe the widely accepted ALD reaction mechanisms that involve the direct interaction of the TMA gas precursor with hydroxylated surface sites. However, as reported by Lakomaa et al. [21] and Puurunen et al. [22], TMA can dissociate on oxygen bridges on both SiO_2 and the Al_2O_3 surfaces. TMA may similarly react with oxygen bridge sites of the TiO_2 surface leading to the following reaction:

$$Ti{-}O^*{-}Ti + Al(CH_3)_3 \rightarrow Ti{-}CH_3 + Ti{-}O{-}Al(CH_3)_2 \quad (5)$$

The succeeding water soaking step will convert the methylated surface species into hydroxylated species. We used XPS to study the change in the chemical state of surface species on the porous TiO_2 layers before and after the ALD reaction. Fig. 2 shows the Ti $2P_{3/2}$ and the Al 2p XPS spectra of the ALD-Al_2O_3/TiO_2 electrode layers as a function of the number of ALD reaction cycles. The XPS spectrum of the as-prepared porous TiO_2 layers [Fig. 2(a)] indicates that the Ti $2p_{3/2}$ core level is situated at 458.9 eV for the anatase layer and 458.8 eV for the rutile layer. Both the peak positions fall within the range reported for TiO_2, which is between 458.8 and 459.4 eV [23]. The binding energy of the Ti $2p_{3/2}$ electron of the anatase layer first red-shifts to 458.4 eV at the first deposition cycle of the Al_2O_3 overlayer, and then gradually blue-shifted to 458.9 eV with increasing the cycle number up to 30-cycles. This observation suggests that an interfacial reaction occurs on the anatase nanoparticles during the deposition of the ALD-Al_2O_3 overlayer. The interfacial reaction on the anatase layer is more evident in the Al 2p spectra shown in Fig. 2(b). The Al 2p peak for the anatase layer after one ALD cycle is situated at 74.1 eV, and the peak shifts to 74.7 eV after 30 cycles of deposition, which is consistent with the reported energy for Al_2O_3 [23]. On the other hand, the Al 2p peak for the rutile layer is situated around 74.1 eV after the first ALD cycle and varied little in the energy position through the 30 cycles of ALD-Al_2O_3 deposition. We have previously shown that these binding energy shifts were a result of the formation of Ti–O–$Al(OH)_2$ surface species on anatase nanoparticles [9,24]. The Ti–O–$Al(OH)_2$ species are produced when the TMA and H_2O precursors react sequentially with the hydroxylated surface of the anatase nanoparticles as described by Eq. (2). The Ti–O–Al(OH)–O–Ti structure should also be formed on the sample surface during the initial stage of the ALD reaction, and it must be responsible for the energy shift of Ti $2p_{3/2}$ electrons as well.

Fig. 3 shows the TEM images of TiO_2 particles featuring a 10-cycle ALD Al_2O_3 overlayer. The TiO_2 nanoparticles separated from the anatase layer have a diameter of ~20 nm (Fig. 3(a)), and those from the rutile layer have a diameter of ~300 nm (Fig. 3(b)). The presence of the Al_2O_3 overlayer is evident in the TEM images. In a previous paper, we

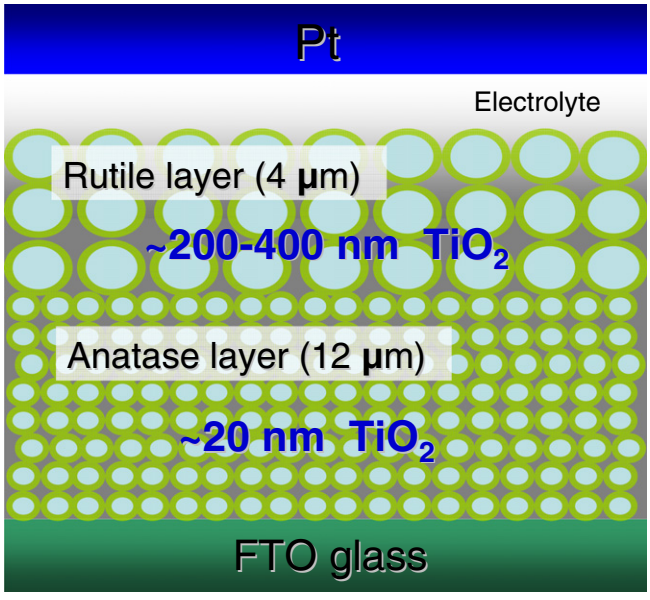

Fig. 1. Schematic illustration of the layer structure of the DSSCs.

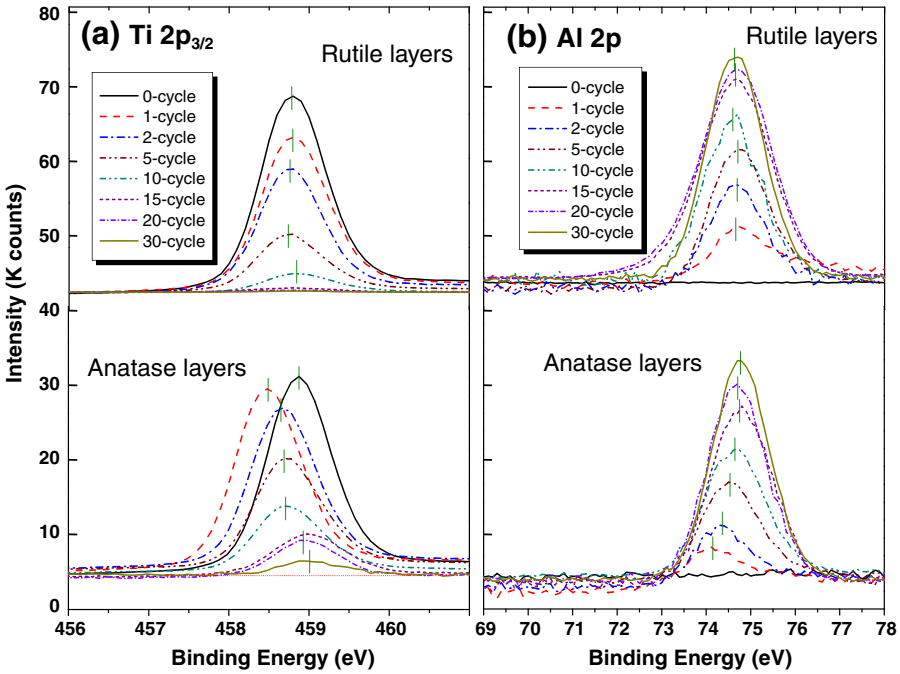

Fig. 2. XPS spectra of the (a) Ti $2p_{3/2}$ and (b) Al 2p electrons for the ALD-Al_2O_3 coated TiO_2 electrodes.

have presented high resolution TEM (HRTEM) images of the TiO_2 nanoparticle featuring an Al_2O_3 overlayer prepared with one, two and five ALD cycles [18]; the HRTEM images showed the formation of islands in the first few ALD cycles. We used TEM to determine the average thicknesses of the ALD Al_2O_3 overlayer prepared with different ALD cycles (Table 1) [18]. Each thickness value listed in the table is the average value of ten TEM measurements at different locations on a TiO_2 particle. The deposition rate (nm/cycle) for the ALD Al_2O_3 overlayer on anatase nanoparticle is 0.14–0.25 nm/cycle, and that on the rutile particle is 0.46–0.52 nm/cycle. It should be noted that the deposition rate for the anatase electrode is likely overestimated because the selection of Al_2O_3 islands from the TEM image for the average thickness evaluation is arbitrary, and higher islands, which are more discernable in the TEM image, are more probably selected for the thickness measurement. The overestimation is particularly true for the first two ALD reaction cycles since discrete Al_2O_3 islands are randomly scattered on the anatase nanoparticle.

The growth mode can be described in terms of the growth-per-cycle (ΔC_m) of the ALD Al_2O_3 overlayer by the following equation [25]:

$$\Delta C_m = \Delta h \times (\rho N_A / M) \quad (6)$$

where ΔC_m is the number of atom m (in this case, Al) adsorbed per unit area of the overlayer per cycle, Δh is the thickness increment per cycle, ρ is the density of the overlayer, N_A is the number of atoms per mole (6.02214×10^{23} mol^{-1}), and M is the molar mass of $AlO_{1.5}$. For an appropriate ρ value, we refer to the literature data for Al_2O_3 ALD films grown using 300 reaction cycles on Si(100) substrates at 150 °C [15]. By substituting the values of ρ (2.9×10^{-21} g/nm^3) and M (50.98 g/mol) into Eq. 6, we obtain the plot for the growth-per-cycle (ΔC_{Al}) of the Al_2O_3 overlayer as a function of the number of ALD reaction cycles as shown in Fig. 4. As discussed previously, the average thickness of the Al_2O_3 overlayer on the anatase electrode was overestimated by TEM images for the first few ALD cycles; hence the ΔC_{Al} values

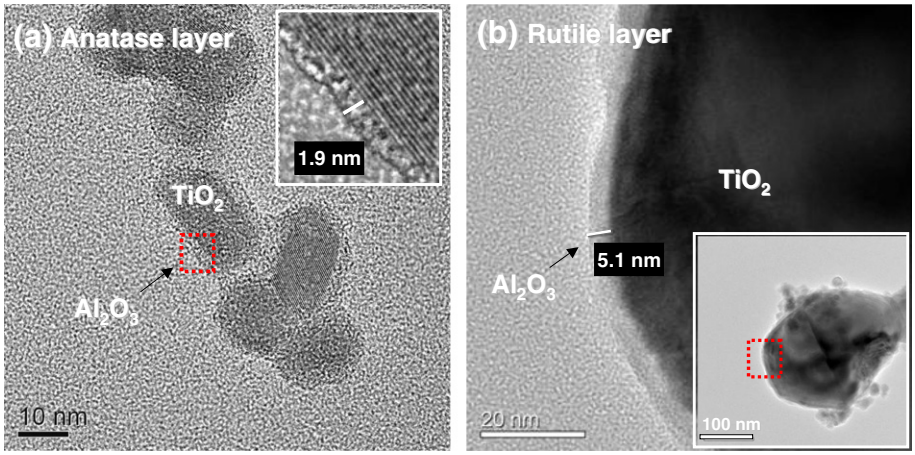

Fig. 3. TEM images of (a) anatase TiO_2 nanoparticles and (b) rutile TiO_2 particles separated from the TiO_2 electrode; both types of the TiO_2 particles were with a 10-cycle ALD Al_2O_3 overlayer. Inset: the high-magnification image of a selected area in (b).

Table 1
Average thicknesses and deposition rates of ALD Al_2O_3 overlayers on TiO_2 electrodes as a function of the number of the ALD Al_2O_3 deposition cycles [18].

Samples		0-cycle	1-cycle	2-cycle	5-cycle	10-cycle	15-cycle	20-cycle	30-cycle
Anatase	Thickness (nm)	0	0.2	0.5	1	1.9	2.5	2.8	4.5
	Deposition rate (nm/cycle)	–	0.2	0.25	0.2	0.19	0.17	0.14	0.15
Rutile	Thickness (nm)	0	0.5	1	2.6	5.1	7.5	9.8	13.8
	Deposition rate (nm/cycle)	–	0.5	0.5	0.52	0.51	0.5	0.49	0.46

presented in Fig. 4 must be larger than the true values. However, the curve profile of the anatase electrode in the figure may still reflect the trend of the variation in the ΔC_{Al} with the number of ALD cycles. The growth-per-cycle increased to a maximum and then decreased to a steady value. This growth behavior is associated with the substrate-inhibited growth mode for the ALD Al_2O_3 overlayer as proposed by Puurunen [26]; the substrate-inhibited growth mode is a result of the island growth on the TiO_2 substrate. The development of islands on the TiO_2 nanoparticle in the first few ALD cycles has been demonstrated by the HRTEM images presented in our previous work [18]. The layer-by-layer growth replaces the island growth to become the main growth mode after 10 cycles of the ALD reaction.

According to Fig. 4, the island growth on the rutile layer is much less obvious than on the anatase layer in the first 5 cycles of the ALD reaction. It has been pointed out by Puurunen that the growth rate of Al_2O_3 is mostly determined by the size of the CH_3 ligand [25] and, in theory, the amount of Al atoms/nm^2 deposited on a flat substrate varies from 4 to 6. Therefore, the self-limited ALD reaction process cannot explain such a large ΔC_{Al} (~18 Al/nm^2) for the rutile electrode. These large ΔC_{Al} values indicate that conventional chemical vapor deposition (CVD) reactions may also occur concurrently during the ALD process. Because of the large rutile particle size of sub-micrometer scale, the rutile electrode must have a very porous framework, which allows more H_2O adsorption and condensation during the water soaking step, and thus makes a complete removal of H_2O by the successive Ar purge more difficult. It is likely that H_2O molecules slowly diffusing out of pores may react with TMA molecules during the TMA soaking step, resulting in the CVD growth of Al_2O_3. As a result, the growth rate of the Al_2O_3 overlayer on the rutile electrode is much larger than that where the overlayer deposition is only via ALD reactions.

The plot in Fig. 4 indicates that the growth mode changes from the island growth mode to the layer-by-layer growth mode on the anatase TiO_2 electrode layer. An immediate thought for the transition is that, after a certain number of ALD cycles, island coalescence results in a continuous Al_2O_3 overlayer, which provides a homogeneous surface for uniform ALD deposition. However, the cause of the island growth during the first few cycles still requires an explanation. The film growth mechanism is mainly decided by the variation in the total energy of the deposited material and the substrate. For Volmer–Weber growth, i.e., island growth, the film growth mechanism is governed by the surface energy of the deposit and substrate, the interfacial energy between the deposit and substrate, and the strain energy accumulated in the deposit and substrate. The relation among these energies can be described by the following expressions [27]:

$$\sigma_s < \sigma_o + \sigma_i + \sigma_{st} \quad (7)$$

$$\sigma_s > \sigma_o + \sigma_i + \sigma_{st} \quad (8)$$

where σ_s is the surface energy of the substrate, σ_o is the surface energy of the overlayer, σ_i is the interfacial energy, and σ_{st} is the accumulated strain energy. These energies vary with the coverage of the deposit under a dynamic film deposition condition. When σ_s is less than the sum of σ_o, σ_i, and σ_{st}, the overlayer is grown via the island growth mode. On the other hand, when σ_s is greater than the sum of σ_o, σ_i, and σ_{st}, the overlayer is grown via the layer-by-layer growth mode. The accumulated strain energy changed with the amount of material deposition, and is an important factor that reverses the inequality in the formula.

To study the effect of the lattice strain on the Al_2O_3 growth mode transition, we used XRD to measure the lattice constants of the anatase and rutile layers as a function of the number of ALD cycles. The XRD specimens were prepared by depositing the anatase and the rutile layers separately on the FTO glass substrate. Fig. 5 shows the XRD patterns of the two samples over a scan range from 24 to 28°. The Bragg's angles of the (101) plane of standard anatase (JCPDS Card Number 21-1272) and the (110) plane of standard rutile (JCPDS Card Number 21-1276) are also provided as marked by the vertical dashed–dotted lines. When the thickness of the Al_2O_3 overlayers

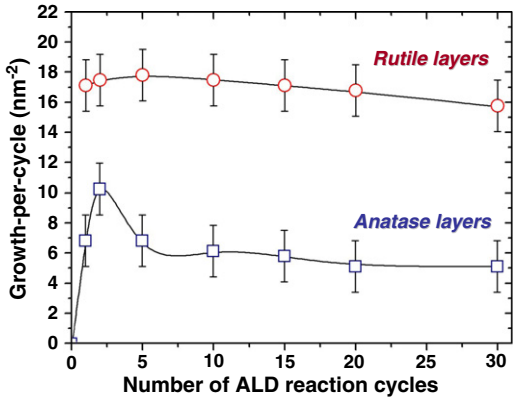

Fig. 4. The plot of the growth-per-cycle of the Al_2O_3 overlayer as a function of the number of ALD cycles of the Al_2O_3 deposition.

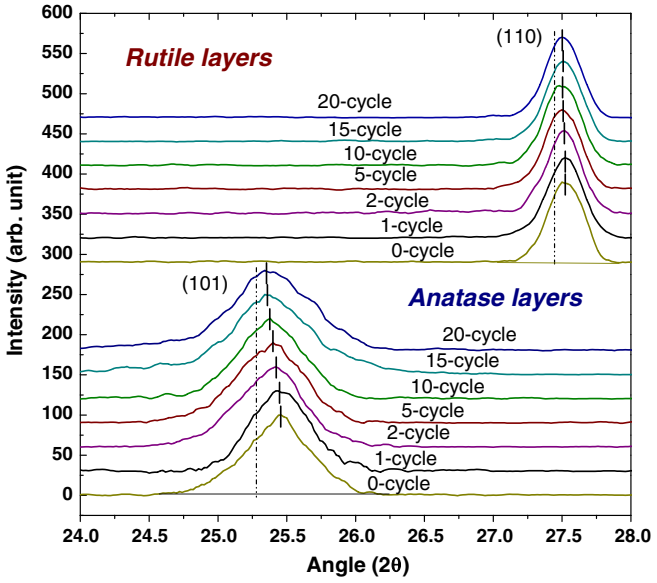

Fig. 5. XRD patterns of (a) the anatase and (b) the rutile electrode layers as a function of the number of ALD cycles of the Al_2O_3 deposition.

Table 2
Lattice constants and lattice volumes of TiO_2 electrodes as a function of the number of ALD Al_2O_3 deposition cycles.

Sample		0-cycle	1-cycle	2-cycle	5-cycle	10-cycle	15-cycle	20-cycle
Anatase	Lattice constants a/c (Å)	3.77/9.41	3.78/9.44	3.77/9.46	3.78/9.47	3.77/9.49	3.77/9.51	3.77/9.51
	Lattice volume (Å^3)	134.3	134.9	135.0	135.3	135.4	135.5	135.7
Rutile	Lattice constants a/c (Å)	4.58/2.95	4.58/2.95	4.58/2.95	4.58/2.94	4.58/2.95	4.58/2.94	4.58/2.95
	Lattice volume (Å^3)	62.0	61.9	62.1	61.9	62.1	62.0	62.0

increases, the (101) diffraction peaks for the anatase sample shift to lower angles, whereas the (110) diffraction peak for the rutile sample remains unchanged. The diffraction peaks for both samples are located at a higher angle than those of the standard samples, suggesting that the TiO_2 lattice might suffer from the stress of contraction. Table 2 lists the lattice constants and lattice volumes of the TiO_2 particles with respect to the number of ALD cycles for the Al_2O_3 deposition. The lattice constant a of the anatase nanocrystal remains almost unchanged through the 30 cycles of ALD deposition, whereas the lattice constant c increases with the number of ALD cycles.

Based on the lattice constants derived from the XRD data, the lattice volume of the anatase and the rutile crystals is plotted as a function of the number of ALD cycles as shown in Fig. 6. The standard lattice volumes of the anatase and rutile phases (JCPDS data) are also provided as marked by the horizontal dashed–dotted lines. For the rutile electrode layer, the lattice volume varies little with respect to the number of ALD cycles. On the other hand, the lattice volume of the anatase electrode layer increases with increasing the number of ALD cycles until the lattice volume becomes steady at the fifteenth ALD reaction cycle. The difference between the steady lattice volume of the TiO_2 electrode layers and the lattice volume of the TiO_2 standards can be attributed to the contractive stress induced by the oxygen deficiency of the TiO_2 particles [28–30]. Observing a large contractive strain in TiO_2 anatase nanocrystals, Li et al. [31] suggested that extensive surface hydration, producing Ti–OH surface species, was the primary cause leading to a smaller lattice constant for the anatase nanocrystal than for its bulk counterpart. Likewise, Ti–OH surface groups on the as-prepared TiO_2 anatase nanoparticle of this study may induce lattice contraction in the nanoparticle as indicated by the large difference in the lattice volume between the as-prepared nanoparticle and the bulk counterpart (Fig. 6). The formation of Ti–O–Al$(OH)_2$ surface species in the first few ALD cycles can relax the surface lattice strain of the TiO_2 nanoparticle as a result of the replacement of Ti–OH moieties via the reactions described by Eqs. (1) and (2). In succeeding ALD reaction cycles, TMA may preferentially react with surface sites of smaller lattice strain, leading to the island growth. The amount of Ti–OH surface species on the anatase nanoparticle gradually decreases in the first few cycles of the ALD-Al_2O_3 deposition, which transforms the Ti–OH surface species into the Ti–O–Al$(OH)_2$ surface groups. As a consequence, the strain energy of the anatase TiO_2 nanocrystal is reduced upon increasing the number of the Al_2O_3 deposition cycle. The lattice strain is minimized when the Ti–OH species are completely consumed, and the ALD-Al_2O_3 deposition becomes homogenous all over the surface of the nanoparticle. If the decrease in the strain energy is large enough so that the inequality in Eqs. 7 and 8 is reversed, the transition from the island growth mode to the layer-by-layer growth mode may occur.

The contractive surface stress should primarily affect the surface lattice of a few atomic monolayers on a particle. Particles of smaller size must have a larger lattice contraction in the particles because of a larger surface to volume ratio. Since the anatase nanoparticle has a much smaller size (~20 nm) than the rutile particle (~200–400 nm), the surface hydration produces a larger surface strain on the anatase nanoparticle. Therefore, the anatase nanoparticle shows a stronger dependence of the lattice volume on the number of ALD cycles than the rutile particle. In addition to the difference in the growth mode

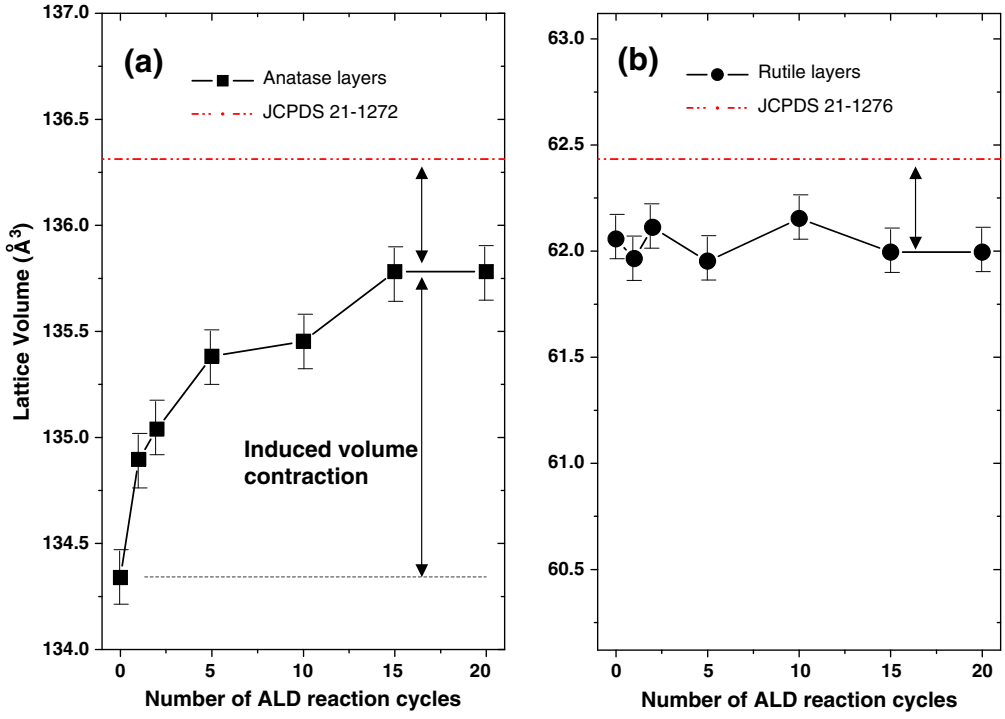

Fig. 6. The plot of the lattice volume of the TiO_2 crystal in (a) the anatase and (b) in the rutile electrode layers as a function of the number of ALD cycles of the Al_2O_3 deposition.

transition between the two TiO_2 electrode layers, the lattice contraction may also affect the ALD-Al_2O_3 deposition rate on the two electrodes. According to Fig. 4 and Table 1, the Al_2O_3 deposition rate on the anatase layer is much smaller than that on the rutile layer before the tenth ALD cycle. Compared with the rutile particle, the anatase nanoparticle has a much larger contractive strain during the first few cycles of the ALD deposition, implying that the first few atomic layers of Al_2O_3 on the anatase nanoparticle are subject to a higher stress, and thus the deposition of these highly stressed atomic layers is energetically unfavorable. However, as discussed previously, because the CVD deposition occurred to the rutile electrode, a clear examination of the influence of the accumulated lattice strain on the growth rate for the rutile electrode is complicated by the CVD deposition. Therefore, a comparison between the two types of electrodes on the effect of the contractive strain on the Al_2O_3 deposition rate is difficult.

According to our previous study, the DSSCs using the porous TiO_2 electrodes have a maximum PCE (6.6%) when anatase nanoparticles are coated by the Al_2O_3 overlayer with a coverage of 0.25, which is achieved after the first ALD deposition cycle [18]. The cause of the low coverage is a result of the prevailing island growth mode during the ALD deposition. The island growth of the Al_2O_3 overlayer results in a low coverage and a non-uniform thickness of the overlayer, and thus greatly degrades the PCE of the DSSCs [18]. Because the contractive strain increases with decreasing the size of TiO_2 particles, it is likely that we can obtain a better PCE for the DSSCs featuring the porous TiO_2 electrode if the size of the anatase nanoparticles is properly increased. When the size of the anatase nanoparticles is correctly chosen to minimize the surface contractive strain, we may obtain a uniform Al_2O_3 overlayer of higher coverage on the anatase electrode during the first few ALD cycles, and thereby the DSSCs may exhibit a better PCE performance compared with those using the present electrode structure featuring anatase nanoparticles of ~20 nm in size.

4. Conclusions

We used a low-temperature (150 °C) ALD process to grow ultrathin Al_2O_3 overlayers on TiO_2 electrodes for the application of dye-sensitized solar cells. The island growth mode was more pronounced on the anatase layer than on the rutile layer at the initial deposition stage, and the layer-by-layer growth mode replaced the island growth mode to become the main growth mode after 15 ALD cycles. The origin of the island growth process is ascribed to the presence of the high surface stress resulting from surface hydration on the TiO_2 nanoparticle at the beginning of the ALD Al_2O_3 deposition. The island growth results in a non-uniform ALD Al_2O_3 overlayer of low coverage on the nanoporous TiO_2 electrodes during the first few ALD reaction cycles. The study suggests that a better PCE of the DSSCs may be obtained if the size of anatase nanoparticles of the DSSC electrode can be appropriately chosen to minimize the surface lattice strain.

Acknowledgment

We thank Miss Chia-Hua Lee (ITRI, Taiwan), Dr Song-Yeu Tsai (ITRI, Taiwan), Miss Su-Jen Chen (ITRI, Taiwan), Miss Iva Chan (ITRI, Taiwan), and the Microstructure and Characterization Laboratory (MCL/ITRI, Taiwan) for technical assistances. This work was under the auspices of the Energy Research and Development Project, Ministry of Economic Affairs (Taiwan, ROC).

References

[1] M. Grätzel, Inorg. Chem. 44 (2005) 6841.
[2] S. Ito, T.N. Murakami, P. Comte, P. Liska, C. Grätzel, M.K. Nazeeruddin, M. Grätzel, Thin Solid Films 516 (2008) 4613.
[3] M. Shanmugam, M.F. Baroughi, D. Galipeau, Thin Solid Films 518 (2010) 2678.
[4] A. Zaban, S.G. Chen, S. Chappel, B.A. Gregg, Chem. Commun. (2000) 2231.
[5] S. Wu, H. Han, Q. Tai, J. Zhang, S. Xu, C. Zhou, Y. Yang, H. Hu, B. Chen, X.Z. Zhao, J. Power Sources 182 (2008) 119.
[6] E. Palomares, J.N. Clifford, S.A. Haque, T. Lutz, J.R. Durrant, J. Am. Chem. Soc. 125 (2003) 475.
[7] X.T. Zhang, H.W. Liu, T. Taguchi, Q.B. Meng, O. Sato, A. Fujishima, Sol. Energy Mater. Sol. Cells 81 (2004) 197.
[8] Z. Liu, K. Pan, M. Liu, M. Wang, Q. Lu, J. Li, Y. Bai, T. Li, Electrochim. Acta 50 (2005) 2583.
[9] T.C. Tien, F.M. Pan, L.P. Wang, C.H. Lee, Y.L. Tung, S.Y. Tsai, C. Lin, F.Y. Tsai, S.J. Chen, Nanotechnology 20 (2009) 305201.
[10] S. Ito, N.L.C. Ha, G. Rothenberger, P. Liska, P. Comte, S.M. Zakeeruddin, P. Péchy, M.K. Nazeeruddin, M. Grätzel, Chem. Commun. (2006) 4004.
[11] S.A. Haque, E. Palomares, H.M. Upadhyaya, L. Otley, R.J. Potter, A.B. Holmes, J.R. Durrant, Chem. Commun. (2003) 3008.
[12] E. Palomares, J.N. Clifford, S.A. Haque, T. Lutz, J.R. Durrant, Chem. Commun. (2002) 1464.
[13] K.M.P. Bandaranayake, S.M.K. Indika, W.P. Prasad, K. Tennakone, Coord. Chem. Rev. 248 (2004) 1277.
[14] J.W. Elam, D. Routkevitch, P.P. Mardilovich, S.M. George, Chem. Mater. 15 (2003) 3507.
[15] M.D. Groner, F.H. Fabreguette, J.W. Elam, S.M. George, Chem. Mater. 16 (2004) 639.
[16] M. Ritala, M. Leskelä, Nanotechnology 10 (1999) 19.
[17] L. Niinistö, J. Päiväsaari, J. Niinistö, M. Putkonen, M. Nieminen, Phys. Stat. Sol. (a) 201 (2004) 1443.
[18] T.C. Tien, F.M. Pan, L.P. Wang, F.Y. Tsai, C. Lin, J. Phys. Chem. C 114 (2010) 10048.
[19] A. Zaban, S. Ferrere, J. Sprague, B.A. Gregg, J. Phys. Chem. B 101 (1997) 55.
[20] C.A. Wilson, R.K. Grubbs, S.M. George, Chem. Mater. 17 (2005) 5625.
[21] E.-L. Lakomaa, A. Root, T. Suntola, Appl. Surf. Sci. 107 (1996) 107.
[22] R.L. Puurunen, J. Appl. Phys. 97 (2005) 121301.
[23] J.F. Moulder, W.F. Stickle, P.E. Sobol, K.D. Bomben, Handbook of X-ray Photoelectron Spectroscopy, Perkin–Elmer Press, Eden Prairie, MN, 1962, p. 45.
[24] C. Lin, F.Y. Tsai, M.H. Lee, C.H. Lee, T.C. Tien, L.P. Wang, S.Y. Tsai, J. Mater. Chem. 19 (2009) 2999.
[25] R.L. Puurunen, Chem. Vap. Deposition 9 (2003) 327.
[26] R.L. Puurunen, W. Vandervorst, J. Appl. Phys. 96 (2004) 7686.
[27] Z. Sitar, L.L. Smith, R.F. Davis, J. Cryst. Growth 141 (1994) 11.
[28] P.P. Ahonen, E.I. Kauppinen, J. Mater. Res. 14 (1999) 3938.
[29] J.C. Parker, R.W. Siegen, J. Mater. Res. 5 (1990) 1246.
[30] E.H. Poniatowski, R.R. Talavera, M.C. Heredia, O.C. Corona, R.A. Murillo, J. Mater. Res. 9 (1994) 2102.
[31] G. Li, L. Li, J. Boerio-Goates, F. Woodfield, J. Am. Chem. Soc. 127 (2005) 8659.